



Contents lists available at ScienceDirect

## Journal of Power Sources

journal homepage: [www.elsevier.com/locate/jpowsour](http://www.elsevier.com/locate/jpowsour)

## Scanning transmission X-ray microscopy of nano structured thin film catalysts for proton-exchange-membrane fuel cells



Vincent Lee<sup>a</sup>, Viatcheslav Berejnov<sup>a,c</sup>, Marcia West<sup>b</sup>, Sumit Kundu<sup>c</sup>, Darija Susac<sup>c</sup>, Jürgen Stumper<sup>c</sup>, Radoslav T. Atanasoski<sup>d</sup>, Mark Debe<sup>d,1</sup>, Adam P. Hitchcock<sup>a,\*</sup>

<sup>a</sup> Brockhouse Institute for Materials Research, McMaster University, Hamilton, ON L8S 4M1, Canada

<sup>b</sup> Faculty of Health Sciences Electron Microscopy, McMaster University, Hamilton, ON L8N 3Z5, Canada

<sup>c</sup> AFCC Automotive Fuel Cell Cooperation Corp., 9000 Glenlyon Parkway, Burnaby, BC V5J 5J8, Canada

<sup>d</sup> 3M Center, 201-2N-19, 3M Company, St. Paul, MN 55144, USA

### H I G H L I G H T S

- STXM is used to analyse nano structured thin film (NSTF) catalyst fabrication.
- STXM is used to follow assembly into a PEM-FC as anode.
- STXM is used to track changes during start-up/shut-down & reversal testing.
- The perylene 149 support of NSTF is lost during these tests.
- Its loss does not affect performance during its lifetime.

### A R T I C L E I N F O

#### Article history:

Received 7 February 2014

Accepted 4 April 2014

Available online 14 April 2014

#### Keywords:

Nanostructured thin film

NSTF

Catalyst layers

PEM-FC

Automotive fuel cells

STXM

### A B S T R A C T

Scanning transmission X-ray microscopy (STXM) has been applied to characterize nano structured thin film (NSTF) catalysts implemented as electrode materials in proton-exchange-membrane (PEM) fuel cells. STXM is used to study all chemical constituents at various stages in the fabrication process, from the perylene red (PR149) starting material, through the formation of the uncoated perylene whiskers, their coated form with Pt-based catalyst, and toward the NSTF anode fully integrated into the catalyst coated membrane (CCM). CCM samples were examined prior to operational testing and after several different accelerated testing protocols: start-up/shut-down (SU/SD), and reversal tests. It was found that, while the perylene support material is present in the pre-test samples, it was completely absent in the post-test samples. We attribute this loss of perylene material to the presence of cracks in the catalyst combined with intensive hydrogenation processes happening at the anode during operation. Despite the loss of the perylene support, the platinum shells forming the NSTF anode catalyst layer performed well during the tests.

© 2014 Elsevier B.V. All rights reserved.

### 1. Introduction

Proton exchange membrane (PEM) fuel cells are a promising alternative to internal combustion engines for automotive applications [1,2]. Typically, the electrodes of the catalyst coated membrane (CCM) of PEM fuel cells are made of nanometer scale Pt catalyst particles (3–5 nm) supported on larger (~50 nm) carbon support particles [3]. In these dispersed catalyst electrodes the

catalyst is distributed more or less evenly over the whole accessible carbon support network and occupies the whole electrode volume. They work well due to the naturally high catalyst active area (~50 m<sup>2</sup> g<sub>Pt</sub><sup>-1</sup> electrochemical surface area – ECSA) and good electrical conductivity of the carbon support (~5 S m<sup>-1</sup>). However, in order to meet the market target [4] for low Pt utilization (less than 0.2 mg cm<sup>-2</sup> Pt loading) the dispersed catalyst electrodes, including Pt loading, are usually optimized with respect to their electrochemical and mass transport functions. The anode, with fast hydrogen oxidation kinetics, requires less Pt than the cathode, for which the oxygen reduction kinetics are several orders of magnitude slower. This means that the anode thickness can be much smaller than the cathode thickness by a factor of 5–10. However,

\* Corresponding author. Tel.: +1 905 525 9140x24749.

E-mail address: [aph@mcmaster.ca](mailto:aph@mcmaster.ca) (A.P. Hitchcock).

<sup>1</sup> Retired.

state-of-the-art carbon supported dispersed catalyst electrodes are highly sensitive to a variety of unwanted degradation processes leading to deterioration of the CCM, in particular platinum dissolution and carbon corrosion [5].

One promising catalyst electrode technology being considered as an alternative to the dispersed Pt/C catalyst electrodes is nanostructured thin film (NSTF) catalyst electrodes [1,3,6–8]. The NSTF catalyst electrodes demonstrate high active area ( $\sim 10 \text{ m}^2 \text{ g}_{\text{Pt}}^{-1}$  ECSA) for sufficiently thin structures ( $\sim 1 \mu\text{m}$  for NSTF versus  $\sim 10 \mu\text{m}$  for dispersed Pt/C catalyst electrodes), which is a result of an initially highly ramified inert support structure made from organic nano-whiskers combined with highly dispersed platinum formed from metallic sub-nano whiskerettes, Fig. 1. The NSTF support layer consists of oriented whiskers of perylene red, PR-149, which are deposited onto a microstructured catalyst transfer substrate (MCTS) and then annealed to form the whisker structure via a screw dislocation growth process [6]. Under most conditions PR-149 whiskers are thermally and electrochemically stable [6–10]. The whiskers are then coated with platinum or platinum alloys to form a manifold of tiny metal whiskerettes ( $\sim 5 \text{ nm}$  in size) with surfaces dominated by  $\{111\}$  facets [11]. To fabricate the catalyst coated membrane (CCM), the catalyst coated side of the NSTF electrode is decal transferred to a perfluorosulfonic acid (PFSA) membrane. Fig. 1 presents scanning electron microscopy (SEM) and transmission electron microscopy (TEM) images of NSTF materials, in the pre-decal whisker-film (Fig. 1a, b), and after decaling to a polymer electrolyte membrane (Fig. 1c–e).

This NSTF catalyst layer technology has been shown in lab tests to provide several advantages over conventional dispersed Pt/C catalyst electrodes. These include: greater stability at higher potentials and higher temperatures, lower peroxide generation, and

higher specific activity for the oxygen reduction reaction (ORR) [6,12]. Due to the replacement of carbon support with PR-149, carbon corrosion events were not expected to occur since PR-149 is an organic photoconductor that does not undergo electrochemical corrosion up to potentials of 2 V relative to a reversible hydrogen electrode (RHE) [6]. Therefore, relative to dispersed Pt/C catalyst electrodes, NSTF catalysts should provide greater tolerance to transitional effects at start-up/shut-down (SU/SD) and cell reversal events. Since NSTF electrodes are much thinner than conventional dispersed electrodes there is no need for ionomer incorporation in the electrode to facilitate proton transport. The high quality of the Pt whiskerette facets makes the electrodes more stable to Pt dissolution and agglomeration which can occur at high potentials. The catalyst phase decorates the high surface area PR-149 whiskers very uniformly with high density of active sites leading to an enhanced specific ORR activity for cathode [3,6]. In addition, fabrication of NSTF electrocatalyst layers is a totally dry process, which reduces the number of steps, improves quality control, eliminates many life cycle management issues and simplifies scale-up [1].

Although NSTF catalyst electrodes still need further material/morphological optimization and development for scale-up they are a very promising alternative to conventional dispersed Pt/C catalyst layers, especially for use as the anode. The fact that NSTF anodes do not have carbon support particles should eliminate some carbon corrosion issues happening during transitional events. Therefore accelerating testing schemes designed to check the durability of the integrated CCM with dispersed Pt/C catalyst cathode and NSTF catalyst anode need to be developed and chemical structure – performance correlations need to be established for these morphologically different electrodes. While the electrochemical

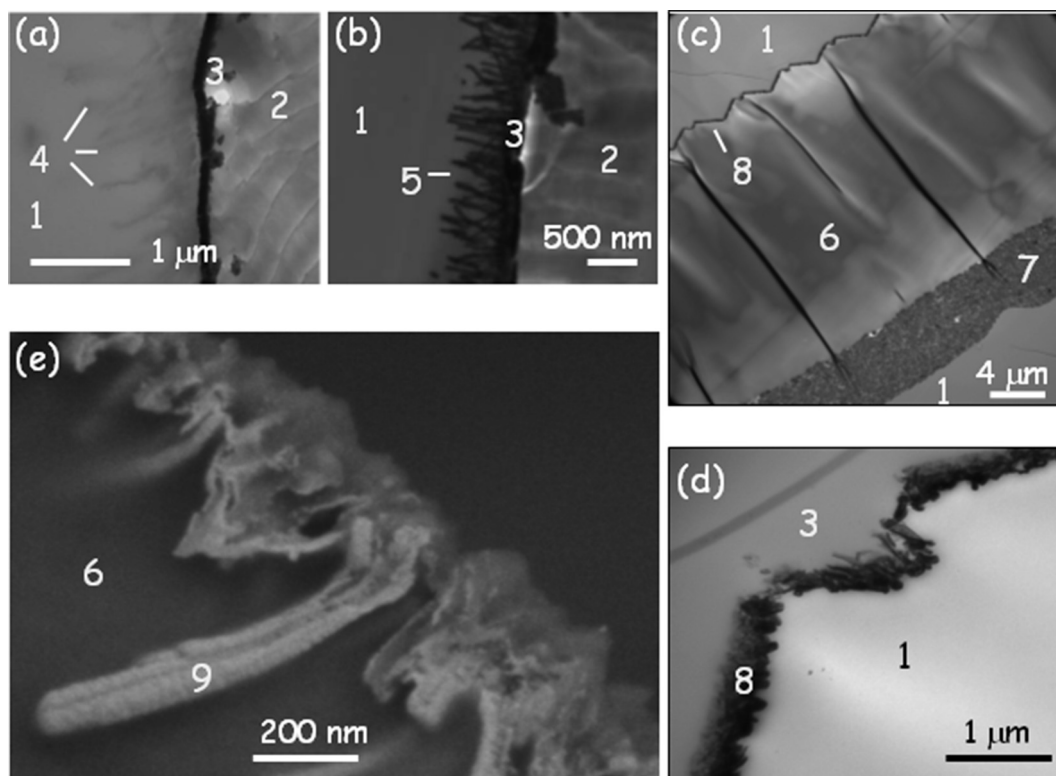


**Fig. 1.** (a–d) TEM and (e) SEM images of the samples examined. Except (e), these are microtome cuts of samples embedded in an epoxy labeled – 1, (a) PR 149 whiskers – 4 grown on a metal release layer – 3 on the microstructured catalyst transfer substrate (MCTS) polymer film – 2. (b) PR149 whiskers coated with Pt – 5. (c) Cross section of the NSTF CCM showing the PFSA membrane – 6, the cathode – 7 and the anode – 8. (d) Expanded view of the NSTF CCM in the anode region showing the deformed, Pt coated whiskers in the anode – 8. (e) SEM of the Pt coated PR 149 whiskers – 9 embedded in the PFSA membrane – 6.

performance of NSTF based PEM fuel cells has been evaluated [6,8,13,14], detailed chemical analyses of the CCM components, in preparation, after integration, as well as before and after durability evaluation, have not been reported previously. Such information could assist in understanding the properties of NSTF based electrodes, potentially leading to further improvement.

Synchrotron based scanning transmission X-ray microscopy (STXM) [15–17] is a powerful tool for characterizing CCM components [18–24] as it provides local chemical speciation via near edge X-ray absorption fine structure (NEXAFS) spectroscopy. STXM can also quantitatively map chemical components in catalyst layers and membrane with 30 nm spatial resolution, providing high sensitivity to the specific structure of the organic as well as the metal components of the electrode-membrane system. Recently, STXM has been used successfully for characterizing ionomer distributions in different catalyst layer structures [22], providing quantitative X–Y maps of the ionomer and carbon support components in the PEM cathodes fabricated by conventional methods using Pt/C nanoparticles [23]. It was also shown that STXM spectro-tomography of PEM fuel cell samples can deliver 3D maps of carbon support and ionomer in the CCM [24].

In this article we report results of an STXM study of the evolution of the morphology and electronic structure of the underlying PR149 electrode support material and associated components, through various stages of NSTF whisker fabrication, processing and operating of the CCMs with integrated dispersed Pt/C cathode and NSTF anode. The pristine PR-149 powder, as-grown whiskers, and an NSTF electrode after attachment to a perfluorosulfonic acid (PFSA) membrane were measured to characterize the processing stages. In addition, we report measurements of the structural changes of PR-149 whisker support for the dispersed Pt/C cathode and NSTF anode integrated CCM that was passed through accelerated SU/SD and reversal tests. STXM was used to study a) the electronic structure of the PR 149 material, while simultaneously imaging the resulting structural transformation it undergoes from the as-grown whiskers morphology to the catalyst coated membrane assembly; and b) the structural and electronic structure changes in the PR-149 material as it passes through different fuel cell testing regimes. A major result is a very dramatic decrease of amount of the perylene support material in the anodes of the EOL samples, to the extent that in one of two test sample preparations, PR 149 could not be detected at all (despite this, the MEA devices performed normally). A preliminary report of the results on the BOL and EOL samples has been presented in an ECS Transaction [25]. This study shows that STXM is a powerful tool for characterizing NSTF electrodes through various fabrication and fuel cell test processes.

## 2. Experimental

### 2.1. Materials, integrated CCMs, and measurements

CCM fabrication was organized in the following way: anode layers were prepared by 3M and integrated into CCM at AFCC. The NSTF whisker layers are fabricated from *N,N*-di(3,5-xylyl)perylene-3,4:9,10bis(dicarboximide), also known as perylene red (PR 149). PR149 is vapor deposited onto a microstructured catalyst transfer substrate (MCTS) that is attached to a support film (Dupont Kapton™) and then is heated in-vacuo to form a monolayer of oriented crystalline whiskers [6] (Fig. 1a, b). The MCTS film used for whisker grow has a corrugated surface with a saw tooth profile (Fig. 1c) that increases the surface area by a factor of 2<sup>0.5</sup> and facilitates roll processing [6]. After the whiskers are formed their surface is coated by vacuum sputtering of Pt to form a whiskerette shell over the perylene whiskers with a target Pt loading of

0.05 mg cm<sup>-2</sup>, and then with oxygen evolution reaction (OER) catalyst containing Ru and Ir with 0.015 mg cm<sup>-2</sup> of the total loading (Fig. 1b). To form the integrated dispersed-NSTF CCMs the catalyst coated side of the NSTF electrode undergoes decal transfer to a 35 μm thick 3M perfluorosulfonic acid (PFSA) membrane (850EW). After transfer to the surface of the membrane the MCTS saw tooth structure is still present (Fig. 1c), but the whiskers are significantly compressed and deformed (Fig. 1d). The resulting CCM anode electrode is only ~0.25 to 1.0 μm thick (Fig. 1d, e). The dispersed Pt/C cathode used a graphitic carbon support and 0.25 mg cm<sup>-2</sup> Pt loading.

The SU/SD and reversal tests were done at the AFCC facility using single MEA testing hardware with active area ~48.4 cm<sup>2</sup>. The SU/SD tests is a four part protocol: 1) air is fed to the cathode and hydrogen to the anode with no load, 2) the anode gas is switched to air resulting in a temporary increase in cathode half cell potentials, 3) the anode gas is switched back to hydrogen resulting in another temporary increase in cathode potentials, 4) a load of 1.0 A cm<sup>-2</sup> is drawn from the cell. The four steps are repeated for 2000 cycles at

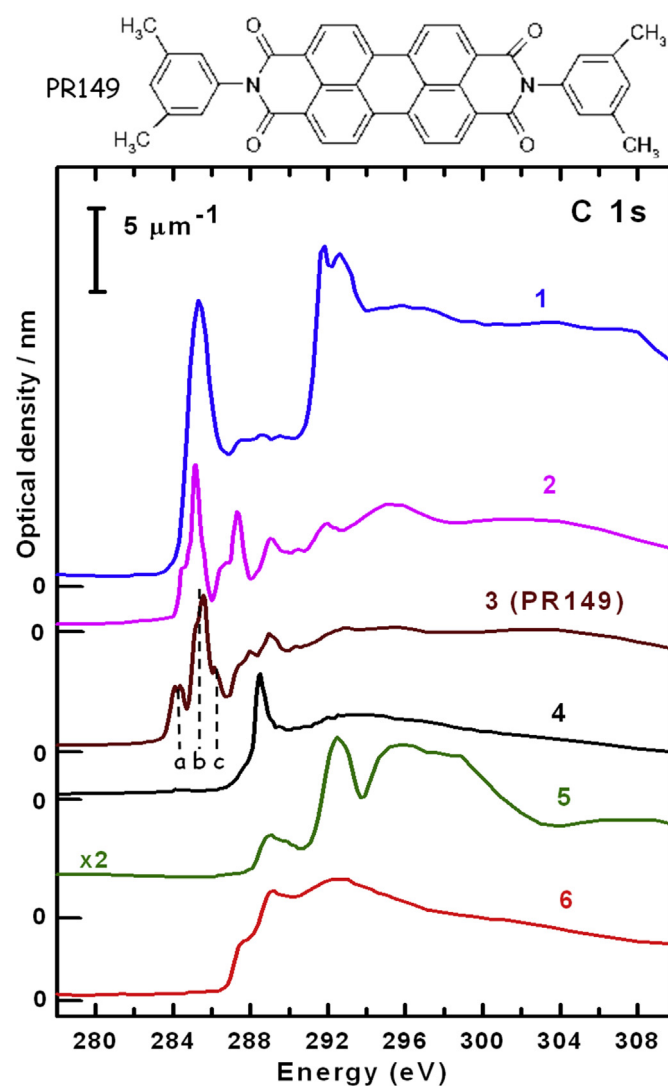


Fig. 2. C 1s spectra of carbon support – 1, Kapton – 2, perylene red powder – 3 (PR149, structure presented at the top of this figure), the microstructured catalyst transfer substrate (MCTS) – 4, perfluorosulfonic acid (PFSA) – 5, and embedding epoxy – 6. The intensity scale is absolute – optical density per nm thickness. Offsets are used for clarity. The characteristic C 1s → π\* peaks in PR149 labeled – a, b, c – occur at 284.2, 285.3 and 286.4 eV respectively. See text for spectral assignments.

100% RH and 68 °C. The reversal tests consisted of feeding fully humidified air and nitrogen to the cathode and anode respectively at 60 °C and drawing a current of 0.2 A cm<sup>-2</sup> for 10 h.

## 2.2. Sample preparation for STXM and ancillary characterization

The PR-149 powder (obtained from 3M) was dispersed in isopropyl alcohol and dropped onto formvar coated TEM grids to prepare the sample for STXM analysis. The as-grown PR-149 whiskers and all subsequently processed samples were embedded in an amine epoxy, and cured at 20 °C for 72 h followed by 60 °C for 7.5 h and lastly 80 °C for 3 h. The embedded materials are then microtomed into 100–200 nm thick cross-sectional slices which are transferred onto formvar coated TEM grids for further TEM and STXM analysis. The bright field transmission electron microscopy

(TEM) images were obtained at the McMaster Faculty of Health Sciences electron microscopy facility using a JEOL 1200EX operating at 80 kV. Scanning electron microscopy (SEM) imaging of anode layers was done with a Hitachi SU8030 operated in back-scattering mode at 2 kV electron beam acceleration voltage.

## 2.3. STXM measurements

Details of the scanning transmission X-ray microscopy (STXM) instrumentation, operating procedures and analysis methodology have been reported in recent reviews [16,17]. Descriptions of specific aspects of the application to fuel cell materials have been presented elsewhere [18–24]. STXM measurements were made at the Canadian Light Source (CLS) 10ID-1 spectromicroscopy (SM) beamline [26] and at the Advanced Light Source (ALS, Lawrence-

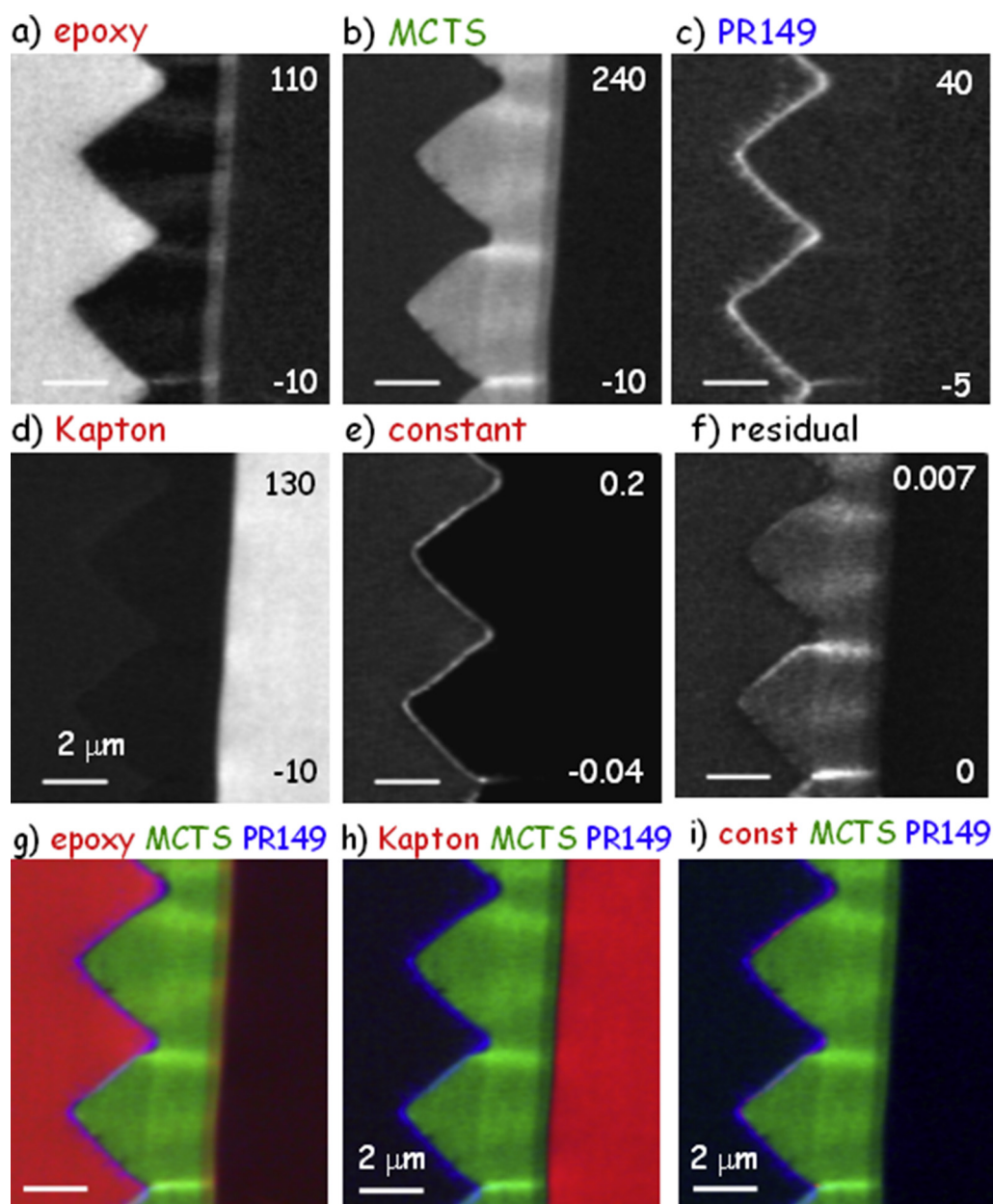


**Fig. 3.** Component maps for (a) epoxy, (b) MCTS, (c) PR149, (d) Kapton and (e) constant (a metal release layer below the PR149 whiskers), derived by a stack fit analysis of a C 1s image sequence measured from an uncoated NSTF whisker sample, grown on MCTS, which is attached to its Kapton support. The numbers on the lower and upper left side of the epoxy, MCTS, PR149 and Kapton images indicate the minimal and maximal thickness in nm, while for constant and (f) residual images, the numbers indicate the minimal and maximal OD values. (g), (h), and (i) are color coded composites (rescaled) of the indicated component maps.

Berkeley National Lab – LBNL) 5.3.2.2 [27,28] beamline. All data was analyzed using the aXis2000 package [29]. Details of the analysis methods have been provided elsewhere [16–24]. Briefly, the thin slices of our materials absorb X-rays to an extent that depends on their local composition and thickness. By imaging these slices at different X-ray energies we are able to see variations of absorption

caused by the material variety or chemical changes due to processing/degradation. The chemical contrast of STXM is based on NEXAFS (near edge X-ray absorption fine structure) spectroscopy [30]. Different elemental edges can be used. Here the results were obtained using image sequences across the C 1s edge to measure spectra at a fine mesh of sample positions [17]. By applying spectral

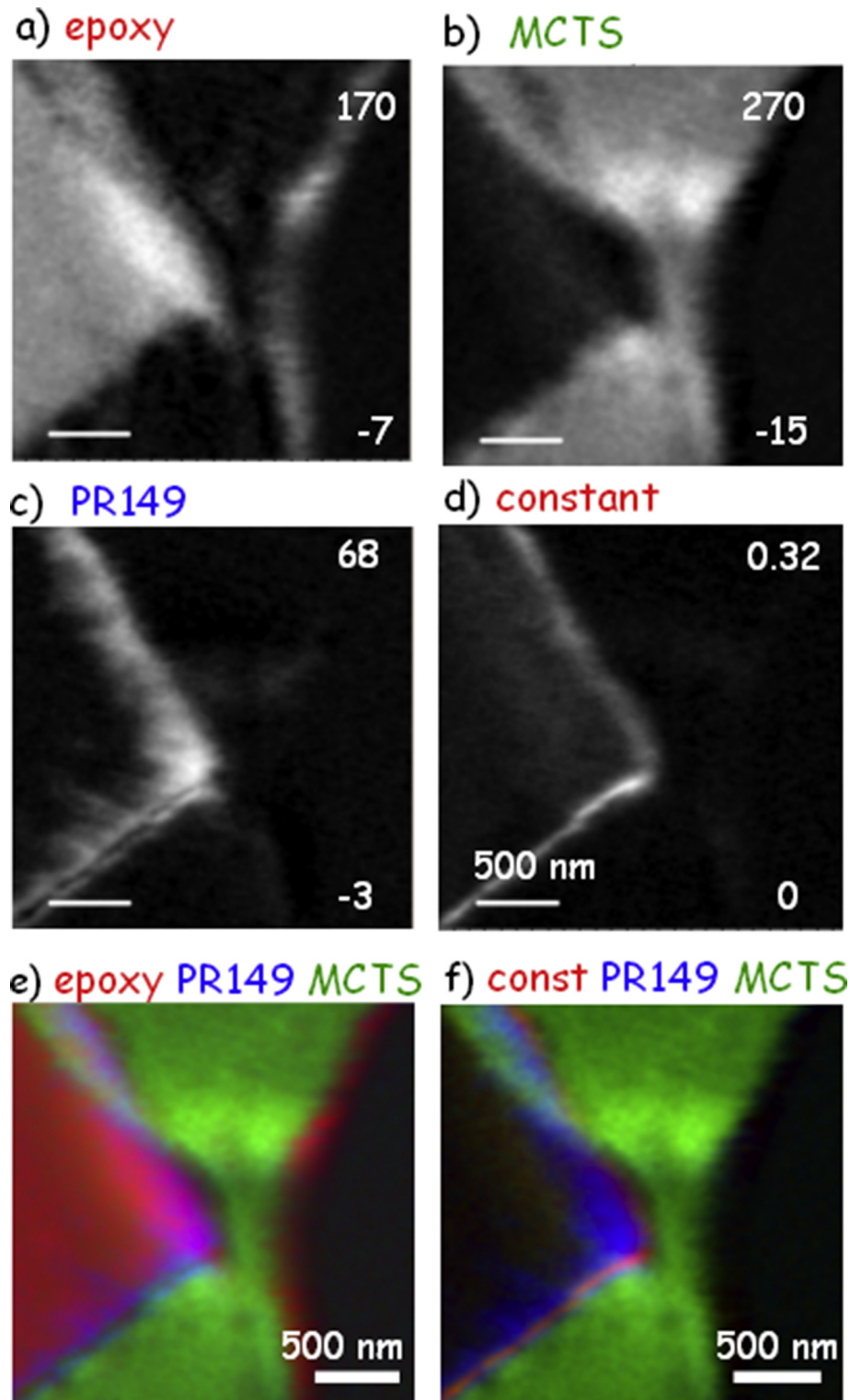


**Fig. 4.** Higher magnification maps and color coded composites for an uncoated NSTF whisker sample. The component maps for (a) epoxy, (b) MCTS, (c) PR149 and (d) constant were derived by a stack fit analysis of a C 1s image sequence. The numbers on the epoxy, MCTS, and PR149 images indicate the minimal and maximal thickness in nm, while that for the constant image indicates the minimal and maximal OD. (e) and (f) are color coded composites (rescaled) of the indicated components.

decomposition methods to the image sequences [17] and using NEXAFS spectra for the pure components for quantitation, we can chemically map the sample to visualize all components (perylene red, carbon, support, catalyst, ionomer), track material changes and correlate these changes back to the fuel cell test conditions.

### 3. Results and discussion

#### 3.1. Spectroscopy survey of the components

Fig. 2 compares the C 1s spectra of dispersed graphitic carbon powder (1), Kapton (2), pure PR-149 powder (3), MCTS acrylate (4), PFSA membrane (5) – OD scale is multiplied by 2, and embedding epoxy (6). The features in these spectra are associated with creating electronically excited states in which electrons from core orbitals have been promoted to orbitals which were unoccupied in the ground state [17,30]. C 1s NEXAFS spectroscopy is particularly useful in this type of study as it can differentiate among the organic materials due to the strong dependence of the spectra of different

carbons on their local bonding environment. The C 1s spectra for all components can be readily differentiated one from another. The C 1s spectrum of PR-149 has similar spectral features to perylene, emphasizing the fused ring core structure [31,32]. The PR-149 spectrum is dominated by C 1s  $\rightarrow \pi^*_{C=C}$  transitions at 284.2, 285.3 and  $\sim 286.4$  eV, with the 3-component structure being related to a combination of delocalization interactions and chemical shifts from the influence of the adjacent heteroatoms – see the chemical formula, Fig. 2. The peak at 288.2 eV arises from C 1s  $\rightarrow \pi^*_{C=O}$  transitions which are observed in PR-149 but not perylene. Broad features at higher energy are attributed to C 1s  $\rightarrow \sigma^*$  transitions. The C 1s spectra of the epoxy and PFSA lack features in the  $\sim 285$  eV region consistent with the absence of C=C double bonds in these species. The feature around  $\sim 289$  eV in the epoxy corresponds to C 1s  $\rightarrow \sigma^*_{C-O}$  transitions, while the shoulder on the lower energy side is due to C 1s  $\rightarrow \sigma^*_{C-N}$  and C 1s  $\rightarrow \sigma^*_{C-H}$  transitions, and the broad peak at  $\sim 293$  eV is associated with C 1s  $\rightarrow \sigma^*_{C-C}$  transitions. The C 1s spectrum of Kapton is very similar to published spectra of polyimides [33,34]. The spectrum is dominated by low lying C 1s  $\rightarrow \pi^*_{C=}$

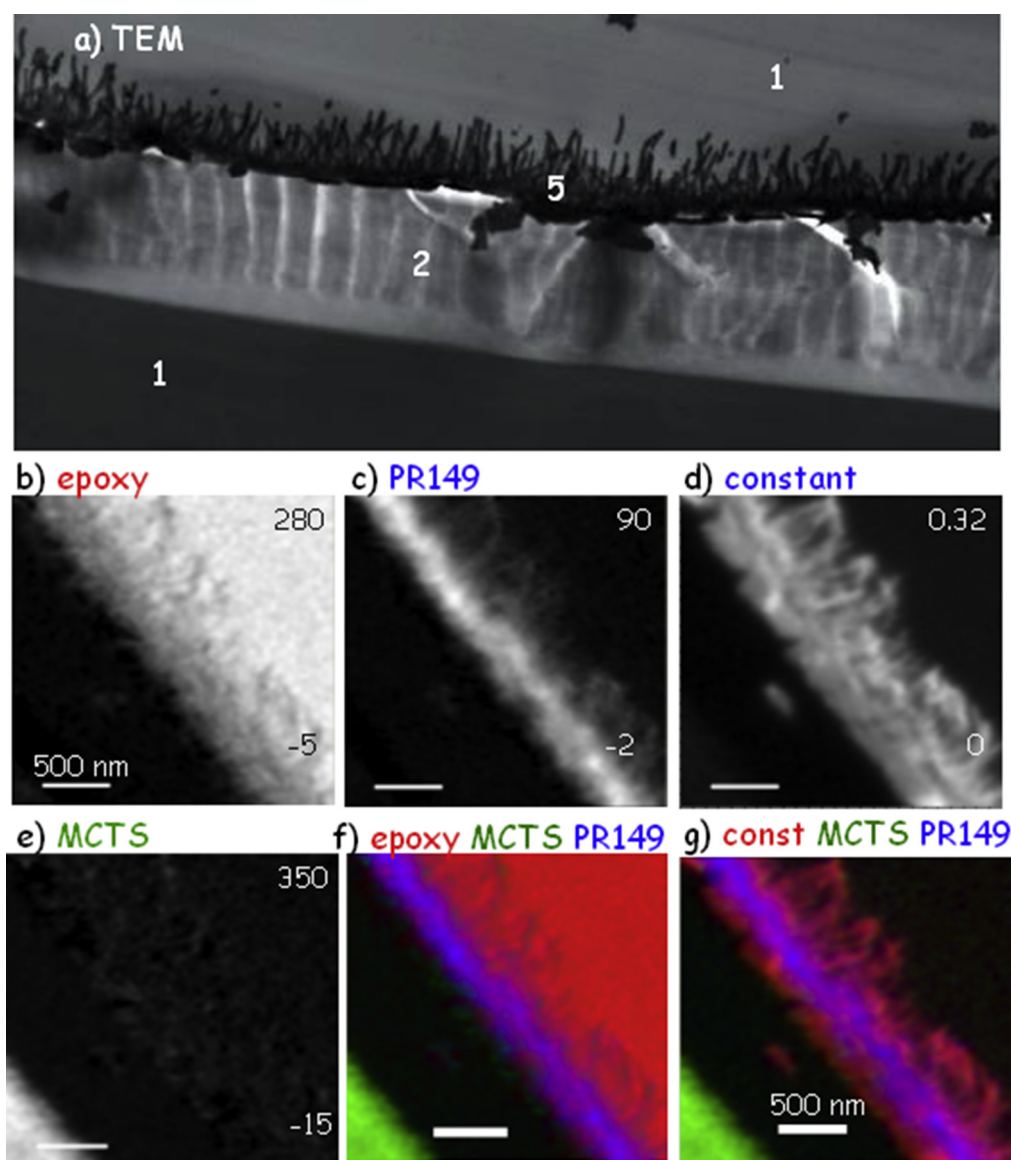


**Fig. 5.** (a) TEM image of the catalyst coated NSTF whiskers – 5 embedded in epoxy – 1, still supported on the MCTS film – 2. (b–e) Component maps for epoxy, MCTS, PR149 and constant, derived by a stack fit analysis of a C 1s image sequence of this sample. The numbers on the epoxy, PR149, MCTS images indicate the minimal and maximal thickness in nm, while that for the constant images indicates the minimal and maximal OD. (e), (f) and (g) are color coded composites (rescaled) of the indicated components.

C and C 1s  $\rightarrow \pi^*_{C=O}$  transitions with energies related to the chemical shifts of carbons attached to the N and O atoms, as well as the  $\pi-\pi$  interactions associated with the extensive  $\pi$ -delocalization. The C 1s spectrum of the MCTS acrylate material (a blend of 1,6-hexanediol diacrylate and dipentaerythritol penta-acrylate) [35] is very similar to the published C 1s spectrum of linear polyacrylates [36]. There are no low-lying C 1s  $\rightarrow \pi^*_{C=C}$  transitions and the spectrum is dominated by the intense C 1s  $\rightarrow \pi^*_{C=O}$  transition at 288.2 eV from the carbonyl site. The C 1s spectrum of the graphitic carbon support (present in the dispersed cathode of the CCM) is very similar to that of graphite [37], with the intense peak at 285 eV arising from C 1s  $\rightarrow \pi^*$  transitions, the sharp peak at 291.8 eV due to the  $\sigma^*$  exciton and the adjacent peak at 292.2 eV from C 1s  $\rightarrow \sigma^*$  transitions.

### 3.2. Spectromicroscopy of the system during preparation

#### 3.2.1. Overview of the NSTF preparation & details of the uncoated whiskers

Fig. 3 presents component maps and color coded composites for a large area of the NSTF sample with uncoated PR149 whiskers on the MCTS support, with its Kapton backing. Fig. 4 presents component maps and color coded composites for an expanded region of this sample. The component maps – gray scale images in both Figs. 3

and 4 – were derived from C 1s STXM image sequences (stacks) by a four component stack fit analysis [17] for the stack presented on Fig. 3 and a three component stack fit analysis for the stack presented in Fig. 4. For these stack fits the quantitative NEXAFS reference spectra of PR-149, embedding epoxy, MCTS support and Kapton substrates were used (Fig. 2). The images labeled 'constant', which is the contribution without any C 1s spectral signature, correspond mainly to a metal layer used in releasing the NSTF whiskers. The units of the gray scale of each component map are thickness in nm, except for the constant and residual images, which the gray scales represent optical density (OD) units. By assigning a color to each of the fitted components, color coded composites are generated (last row of images in Figs. 3 and 4), where the scale of each color has been matched to the full range of thicknesses of each component. The uncoated whiskers are still attached to the MCTS and can be seen clearly in the PR149 component map (Fig. 4c). The spatial resolution of STXM ( $\sim 30$  nm) is sufficient to visualize individual whiskers or their bundles, especially in the regions farthest from the MCTS support film. Fig. 3 illustrates that the NSTF support is made up of two layers of materials. The layer farthest from the PR-149 whiskers is Kapton polyimide material and the layer closest to the whiskers is the MCTS support. Higher magnification TEM micrographs (Fig. 1b–d) show that the whiskers are highly oriented

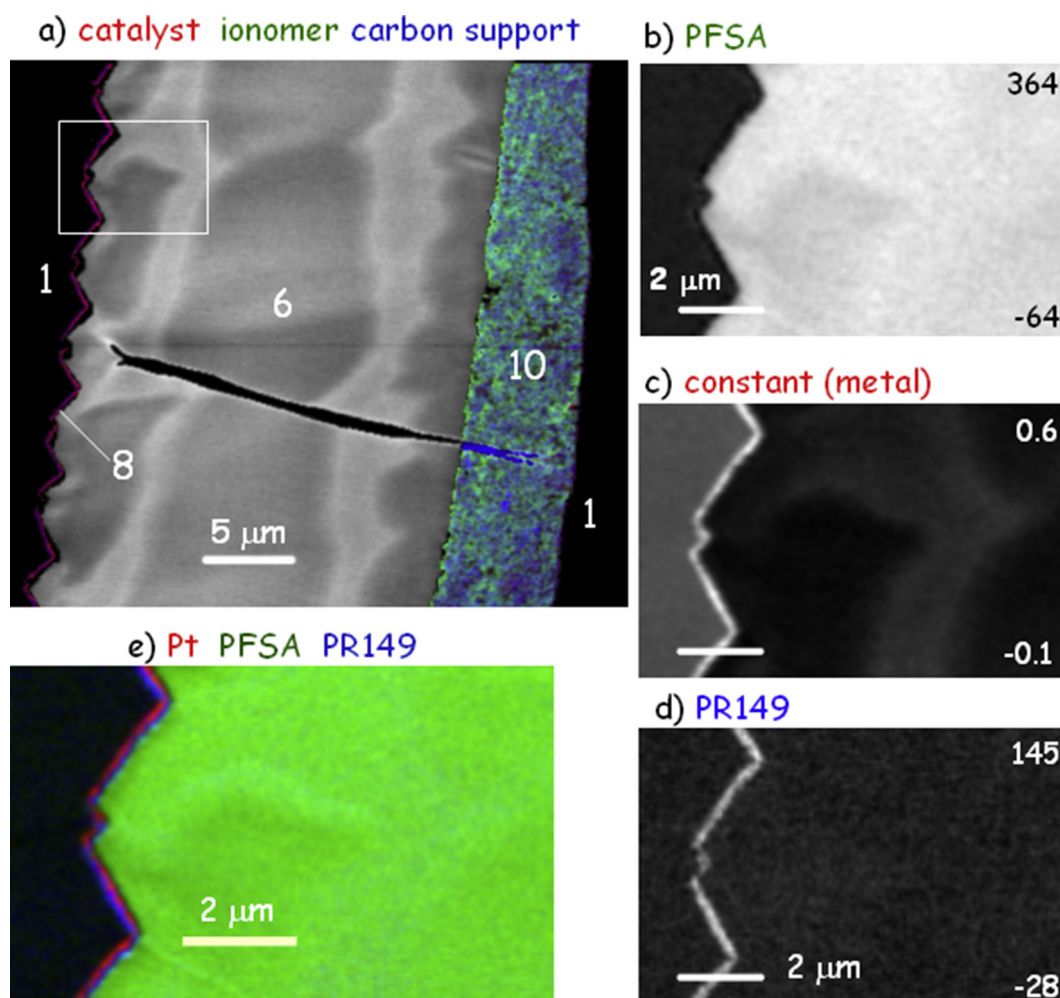


**Fig. 6.** (a) Color coded composite of component maps derived from images of a large area of integrated CCM recorded at four energies (carbon support (blue,  $OD_{285} - OD_{278}$ ), ionomer (green,  $OD_{694} - OD_{684}$ ) superimposed on a gray scale map of the PFSA membrane – 6). This presentation shows the NSTF anode – 8 and dispersed Pt/C cathode – 10, embedded in epoxy – 1. (b–d) Component maps (PFSA, PR149 and constant) of a small area of integrated CCM, derived by a stack fit analysis of a C 1s image sequence measured in the white rectangle in (a). (e) Color coded composite (constant (Pt) – red, PFSA – green, PR149 – blue, all rescaled) for this area. (For interpretation of the references to colour in this figure legend, the reader is referred to the web version of this article.)

and densely packed. The morphology of the whiskers is preserved upon embedding and microtoming as can be seen in the bright field TEM image (Fig. 1a, b). The C 1s spectrum of the PR-149 whiskers is very similar in the  $\pi^*$  energy interval to that of the PR-149 powder (Fig. 2). However, the higher energy features do not match as well in intensity suggesting there may be a structural difference between the whiskers and the powder which may be related to the fact the whiskers are effectively single crystals [6] whereas PR149 powder is an amorphous solid.

### 3.2.2. Catalyst coated whiskers

The morphology of the whiskers is also preserved after catalyst deposition. They are much denser (as indicated by higher contrast in the TEM micrographs, Figs. 1b and 5a) due to deposition of the catalyst metals which are higher electron density materials than carbon polymers. Fig. 5b–e presents component maps while Fig. 5f, g are color coded composites for the catalyst coated whisker sample. The component maps in Fig. 5b–e were derived from a stack fit analysis of a C 1s image sequence using the same material discrimination approach as in Figs. 3 and 4. The constant image here represents the high electron density metal shell on the PR149 whisker core. Since this shell has Pt, Ru and Ir components, which

cannot be discriminated in the C 1s energy interval, the constant map is presented in OD units. Some differences can be observed in the PR-149 whiskers spectra when compared to the powder spectra, (see Fig. 8 for direct comparison). The shoulders around the  $\pi^*$  states are no longer as visible and broadening of the peak centered at  $\sim 289$  eV is observed. These changes in the shape of the  $\pi^*$  peak may be associated with the crystalline nature of the whiskers versus the powder. Similar changes are seen in optical spectra of the aromatic organic solids when they crystallize since the  $\pi^*$  orbitals are directly involved in the intermolecular bonding within the unit cell. The changes could also be due to the presence of catalyst metal that has been deposited on top of the PR-149 whiskers. Metal d-orbitals can interact with  $\pi^*$  states of aromatic materials possibly leading to changes in the overall shape of the  $\pi^*$  peak in PR-149. In addition, vacuum sputtering of the catalyst metal onto the whiskers could have damaged the PR-149 during deposition, further changing its chemical and electronic structure.

### 3.2.3. Integrated CCM (pre-test): dispersed cathode – NSTF anode

Fig. 6 displays results from an integrated CCM sample that has a dispersed cathode (4), an NSTF anode (2) and a PFSA membrane (3). Fig. 6a shows a large area color coded composite of the CCM where a four energy stack map approach [17] was used to map the catalyst metal, graphitic carbon support, epoxy and PFSA ionomer in the electrodes (see the reference spectra on Fig. 2). Fig. 6b–d are component maps for the PFSA, PR149 and the constant (associated with the Pt–Ru–Ir catalysts) from a 4-component stack analysis of a full C 1s image sequence recorded in the region marked as a white

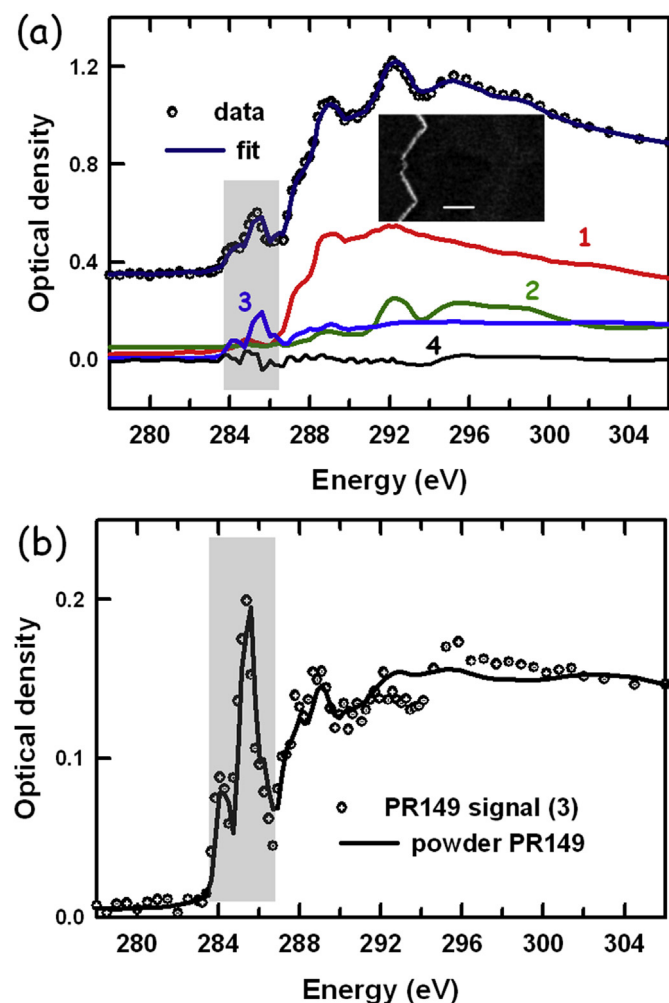


Fig. 7. (a) Fit of the C 1s spectrum of the anode extracted from all pixels with more than 11 nm of PR149 in the component map (see the insert). The fit components are epoxy – 1, PFSA – 2, PR149 – 3 and constant (not shown). 4 is the residual of the fit. (b) Comparison of the PR149 part of the anode spectrum derived by subtracting the epoxy, PFSA and constant components from the anode spectrum. The spectrum of 21 nm of pure PR149 (powder) is also plotted for comparison.

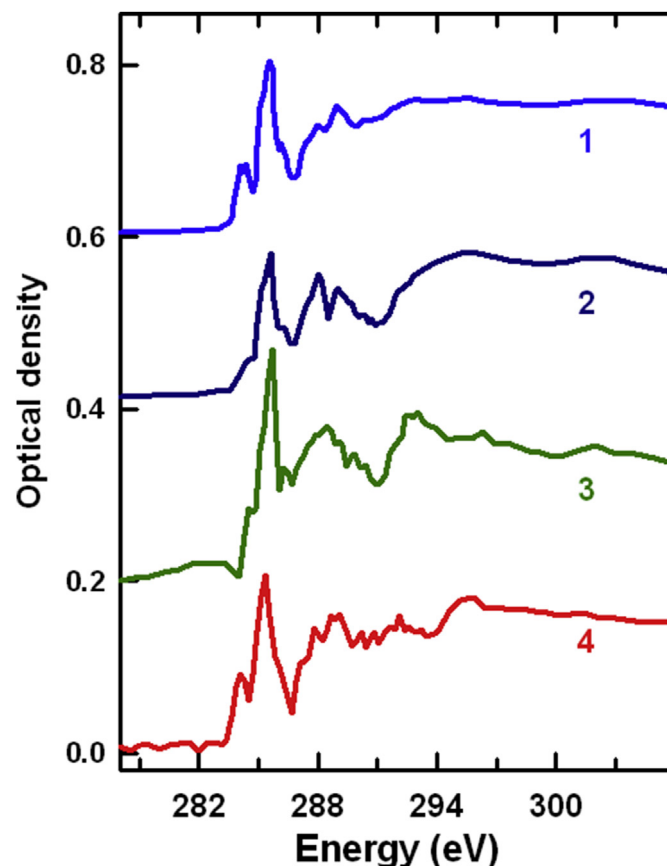


Fig. 8. C 1s spectrum of pure PR149 (1) compared to the C 1s spectra of the PR149 components extracted from (2) the uncoated whisker, (3) the catalyst coated whisker and (4) the anode of the integrated dispersed-NSTF electrode in the CCM sample, (optical density units). Offsets are used for clarity.

rectangle on Fig. 6a (the epoxy map is not shown). Fig. 6e is the color coded composite of the component maps for PR149, PSFA, and constant maps. In principle one expects the perylene support signal to be predominantly on the side of the anode opposite to the PFSA membrane. However this analysis shows that although there are regions like that, in other areas the anode has a relatively uniform purple tinge indicating intimate mixing of the PR149 whisker and the catalyst, while in other areas it seems the catalyst rich part is facing away from the membrane. This is consistent with a high degree of mechanical deformation of the anode when it is decalced on to the membrane.

In order to further analyze the amount of PR149 in the anode of the pre-test sample, the spectrum of the anode specific ROI (see the inset in Fig. 7a) has been isolated by masking the PR14 component map (Fig. 6c) and subjecting the extracted spectrum to spectral fitting. The spectrum of the anode region is plotted in Fig. 7a, along with a spectral decomposition into epoxy (1), PFSA ionomer (2), PR149 (3). The overall spectrum of the anode is more complex than that of the pure PR-149 powder. However, the characteristic double peaked structure of the C 1s  $\rightarrow \pi^*$  transitions in the 284–286 eV region is still evident and a PR-149 (curve 3) component is needed to obtain a satisfactory fit. It is clear that there has been extensive infiltration of the embedding resin (curve 1) and there is also significant contribution from the PFSA signal (curve 2) in the anode layer. PFSA may have been introduced into the whisker layer due to the hot pressing decal transfer step when the membrane in close proximity to the NSTF catalyst layer undergoes self extrusion and fills the porous uncompressed whisker region. The C 1s spectrum of the support material in the compressed and decalced layer of catalyst coated whiskers was isolated from the total spectrum of the anode by subtracting the fitted epoxy, constant and PFSA components. Fig. 7b compares that isolated signal to the spectrum of pure PR149 powder. A good match is observed indicating the perylene support material is

essentially unchanged by the whisker fabrication, metal deposition, and processing into a working CCM.

### 3.3. Evolution of the C 1s spectrum of the whisker support material

The overall changes in the C 1s spectra of the whisker support material through the various stages of the fabrication are summarized in Fig. 8: the pure PR-149 powder (1), uncoated whiskers (2), whiskers coated with catalyst (3) and the signal extracted from the NSTF anode integrated to the real CCM (4). The characteristic  $\pi^*$  features in the 284–286 eV region are evident in all of these spectra suggesting that the aromaticity of the ring structure has been preserved during the processing steps. To some extent features in the 288–300 eV region have broadened or changed which suggests there may have been modifications to the intermolecular packing and longer range structure, to which that energy region is more sensitive. We note that the absolute intensity of the PR149 components is rather similar through the series of samples, suggesting that, although it gets masked by the presence of other organic components in the same spatial region, the PR149 whisker material stays more or less the same all the way through the fabrication and decaling process.

### 3.4. STXM characterization of the NSTF anodes after SU/SD and reversal tests

Fuel cell stacks may encounter specific operational conditions that can significantly accelerate corrosion of the carbon support for dispersed Pt/C catalyst electrodes. Without proper support Pt catalyst nanoparticles move and eventually experience conditions where they can dissolve and coalesce irreversibly [38] which reduces the electrocatalytically active area and permanently lowers the overall fuel cell performance. These specific conditions are associated with transitional regimes of feeding the fuel cell with

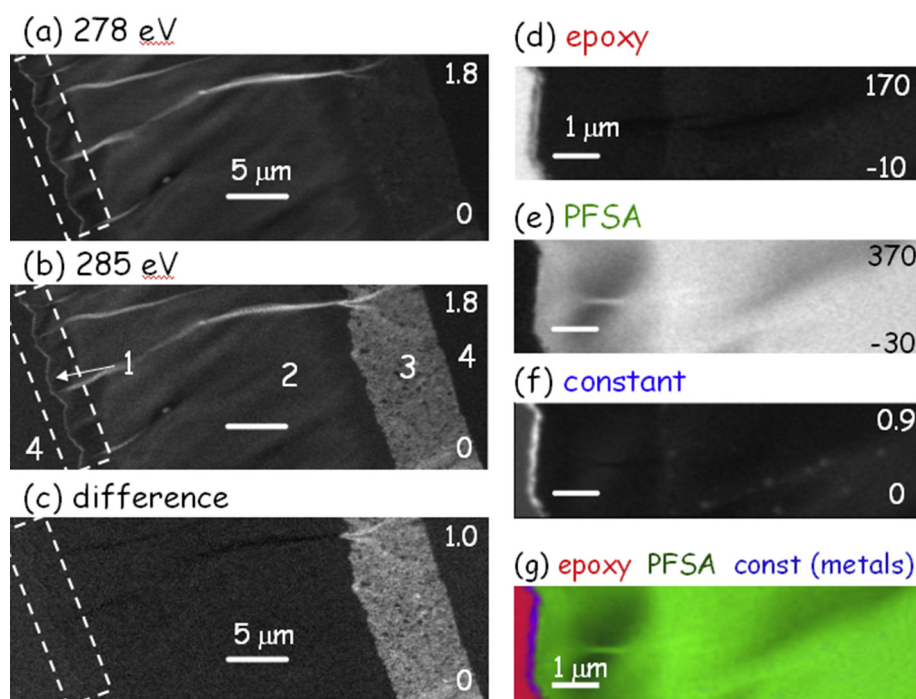


**Fig. 9.** (a–c) Optical density (OD) images of the post-test integrated CCM after reversal testing recorded with STXM at (a) 278 eV, and (b) 285.2 eV. (c) The difference of (b) and (a) images. This is a map of aromatic components which should reveal both the graphitic like support in the dispersed Pt/C cathode and the perylene support in the NSTF anode. The absence of signal in the anode region is direct evidence for chemical transformation or loss of the perylene red support during the reversal testing. (d–f) Component maps derived by fit to a C 1s image sequence. (d) epoxy, (e) PSFA membrane and (f) constant (metal). (g) Color coded composite (rescaled) of epoxy (red), PSFA membrane (green) and constant (metal, blue) components. Perylene red was not detected. (For interpretation of the references to colour in this figure legend, the reader is referred to the web version of this article.)

hydrogen and air (oxygen) [39,40]. In particular, irregularity of gas distribution in the fuel cell electrodes occurs either during the fuel cell stop and start events (SU/SD) or when a particular cell is not performing well and becomes overpowered by the rest of the stack (reversal condition). In the SD regime hydrogen in the dispersed

porous anode is gradually replaced by air (for SU this is opposite) due either to reactant cross-over or by air filling the gas feed flow channel manifold. When a hydrogen/air boundary is formed it then propagates through the flow channels, unevenly feeding the porous anode and triggering a high interfacial potential difference in the

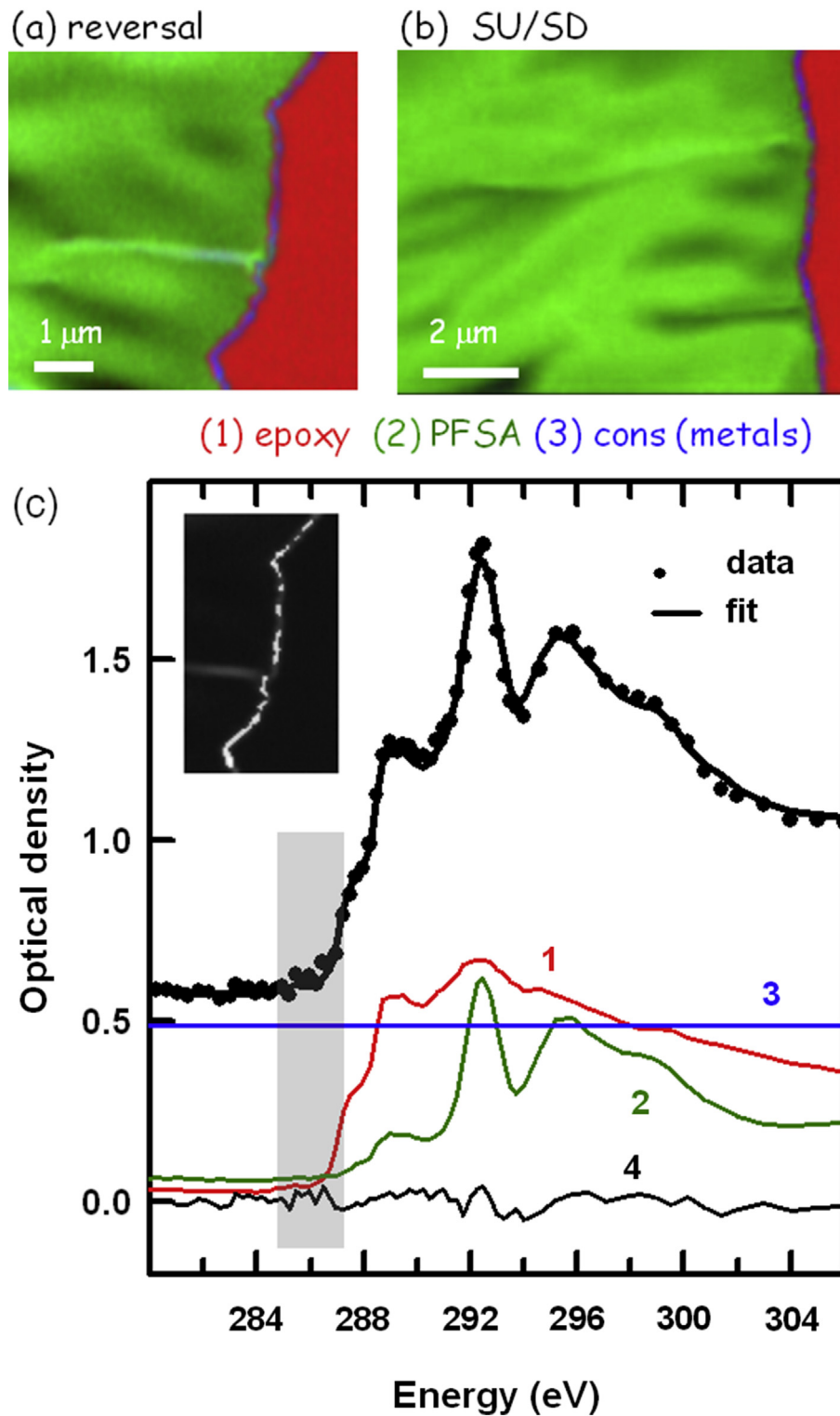


**Fig. 10.** Color coded composite (rescaled) of the epoxy (red), PFSA membrane (green) and constant (metal, blue) components derived by a fit to a C 1s image sequence of: (a) reversal, and (b) SUSD test CCM sample, respectively. (c) Spectrum of the anode extracted from the stack (see inset for location). Perylene red signatures were not detected – see the gray box and compare with Fig. 7. (For interpretation of the references to colour in this figure legend, the reader is referred to the web version of this article.)

region where hydrogen is absent. These events eventually leads to carbon corrosion of the cathode [40]. The reversal regime occurs when one or more cells in a stack experience gross hydrogen starvation. Under such conditions the anode potential becomes elevated to a high positive value and, in the absence of hydrogen, a dispersed Pt/C catalyst anode undergoes carbon support oxidation and water electrolysis [5,40]. In dispersed Pt/C catalyst anodes this type of corrosion causes severe and fast electrode thinning. Since the optimized dispersed Pt/C anodes are thin, tracking this type of corrosion in these mixed CCM cells is important.

The SU/SD and reversal accelerated tests were developed at AFCC for a single fuel cell in order to mimic the major paths for carbon support corrosion. Both tests were applied to CCMs with integrated dispersed Pt/C catalyst as cathodes and NSTF catalyst anodes to compare degradation of these systems with that typical of CCMs fabricated from the dispersed electrodes only. The analysis of differences in degradation properties is out of the scope of this paper and can be found elsewhere [11,41]. Here we want to stress that, unexpectedly, while conducting these tests and performing STXM analysis for pre/post-test samples we found that the PR149 whisker material disappeared from the NSTF catalyst anode.

Post-tested CCM samples with NSTF anodes were characterized by STXM after both reversal and SU/SD tests with the aim to determine the chemical changes that might occur on the anode side as a result of exposure to these accelerated degradation stress conditions. Fig. 9a–c shows large area ( $\sim 40 \mu\text{m} \times \sim 20 \mu\text{m}$ ) optical density (OD) images obtained at (a) 278 eV and (b) 285.2 eV, for the post-tested sample after the reversal test. These two energies were chosen to maximize the PR149 absorption signal to background ratio (see Fig. 2, PR149 spectrum for illustration). The image recorded at 278 eV is before the onset of C 1s absorption for PR149, thus the majority of contrast in the anode and cathode is due to the Pt catalyst. The image recorded at 285.2 eV highlights the PR149 perylene red, as well as the carbon support material in the cathode which is highly graphitic (see Fig. 2). Fig. 9c is the difference of the 285.2 eV and 278 eV OD images which maps the support materials of the anode (1) and cathode (3) only. This is a key image to illustrate our finding. The difference image exhibits negligible contrast in the NSTF anode region (1) suggesting that there has been a loss, or a chemical transformation of the PR149 whisker support material (compare Figs. 9c and 6d).

The absence of PR149 in the NSTF anode region is further supported by component maps derived from fitting a full C 1s stack of the anode region of the integrated CCM, Fig. 9d–g. The spectrum of the post-tested anode after the reversal test fits perfectly to a combination of the embedding epoxy, PFSA membrane, and metal (derived from the constant), without a need to include a PR149 component. Fig. 10a and b presents color coded composites of the component maps for reversal and SU/SD post-tested integrated CCM samples which were obtained as discussed for Fig. 9d–g. Fig. 10c presents the spectrum of the anode region (see inset for the region from which the spectrum was extracted) and its spectral fit. This clearly shows that the post-tested anode after reversal test consists only of the catalyst metal (3) (constant, blue), plus signals from the embedding epoxy (1) (red) and the PFSA membrane (2) (green) which are present in the signal due to the very narrow anode and the finite spatial resolution of STXM. The total fit, shown in black, matches the experimental data very well. The data and the residual (4) in the gray highlighted box has no hint of PR149 or other aromatic signal. This is in distinct contrast to the pre-test sample where the characteristic double  $\pi^*$  structure of PR149 was readily detected (see the corresponding gray highlighted region in Fig. 7). A similar conclusion was obtained by STXM characterization for the anode after SU/SD test; a typical color coded composite of the post-tested NSTF anode region is shown in Fig. 10a.

The disappearance of PR149 support was quite a surprise because, prior to these measurements, it was assumed that PR149 whiskers were inert for wet chemistry. At this point we speculate that PR149 whiskers degrade due to catalytic hydrogenation. Previous studies [40] had confirmed superior performance of NSTF electrodes and, at the same time, the possibility of removing PR149 ex-situ by high temperature annealing while high resolution TEM imaging under Ar and an  $\text{H}_2$  reducing atmosphere [41]. This is the first direct evidence that the PR149 support material could also be deteriorated during operation and that the degradation products are leached out from the NSTF anode leaving Pt shells empty (see the “constant” maps blue color coded on Figs. 9f, g and 10a, b) in a way that is presented in Fig. 3c in [41]. It is known [41] that there are cracks and pinholes in the Pt shell around the whiskers, even prior to decaling. These morphologies are likely enlarged during the decal process in which the NSTF Pt coated whiskers are severely compressed and the precursor layer is detached, opening the base of the whiskers. The presence of cracks and holes in the substantially homogeneous metal catalyst shells gives  $\text{H}_2$  access to the organic PR149 core during operation, possibly leading to catalytic hydrogenation of the PR149 organic material.

#### 4. Summary

STXM has been used to follow the material transformation of the NSTF catalyst support, PR149, through different steps of processing and tests. The NEXAFS spectra suggest that most if not all of the PR-149 is present even after the catalyst metal layer is sputtered on the whisker. Small changes are observed after the catalyst coated whiskers are mechanically compressed and fabricated into an MEA. However, after accelerated stress testing there is essentially no perylene red material remaining. Despite loss of the PR149 support, there is no evidence that its loss affects the catalytic properties of the anode NSTF structure during its life. These studies provide a detailed chemical perspective on the PR149 based NSTF material, how it evolves through fabrication into fuel cell electrodes, and during operation, all factors which ultimately affect the fuel cell performance.

#### Acknowledgments

This work was supported by NSERC (Canada) through Discovery and Collaborative Research and Development grants, the Canada Research Chairs Program and the Catalysis Research for Polymer Electrolyte Fuel Cells (CaRPE-FC) network. STXM studies were carried out at beamline 10ID1 at the Canadian Light Source (CLS), which is supported by the Canada Foundation for Innovation (CFI), NSERC, Canadian Institutes of Health Research, National Research Council (NRC) and the University of Saskatchewan; and at the STXM on beamline 5.3.2.2 at the Advanced Light Source (ALS), which is supported by the Director, Office of Energy Research, Office of Basic Energy Sciences, Materials Sciences Division of the U.S. Department of Energy, under Contract No. DE-AC02-05CH11231. We thank Drs. Jian Wang and Chithra Karunakaran for their expert support at the CLS. We thank Dr. Tolek Tylyszczak and Dr. David Kilcoyne for their expert support of STXM instrumentation at the ALS. We thank Dr. Natalia Kremliaikova for fruitful discussions regarding chemistry of the perylene red transformations.

#### References

- [1] M.K. Debe, *Nature* 486 (2012) 43–51.
- [2] T. Maiyalagan, S. Pasupathi, *Mater. Sci. Forum* 657 (2010) 143–189.
- [3] F.T. Wagner, B. Lakshmana, M.F. Mathias, *J. Phys. Chem. Lett.* 1 (2010) 2204–2219.

- [4] D. Papageorgopoulos, FY 2012 Annual Progress Report DOE Hydrogen and Fuel Cells Program DOE/GO-102012-3767, 2012. V-4.
- [5] R. Borup, J. Meyers, B. Pivovar, Y.S. Kim, R. Mukundan, N. Garland, D. Myers, M. Wilson, F. Garzon, D. Wood, P. Zelenay, K. More, K. Stroh, T. Zawodzinski, J. Boncella, J.E. McGrath, M. Inaba, K. Miyatake, M. Hori, K. Ota, Z. Ogumi, S. Miyata, A. Nishikata, Z. Siroma, Y. Uchimoto, K. Yasuda, K.-I. Kimijima, N. Iwashita, *Chem. Rev.* 107 (2007) 3904–3951.
- [6] M.K. Debe, *J. Electrochem. Soc.* 160 (2013) F522–F534.
- [7] M.K. Debe, in: W. Vielstich, A. Lamm, H.A. Gasteiger (Eds.), *Handbook of Fuel Cells – Fundamentals, Technology and Applications*, John Wiley & Sons, 2003 (Chapter 45).
- [8] M.K. Debe, *J. Electrochem. Soc.* 159 (2012) B54–B67.
- [9] K.K. Kam, M.K. Debe, R.J. Poirer, A.R. Drube, *J. Vac. Sci. Technol. A* 5 (1987) 1914–1916.
- [10] X. Sun, M.S. Saha, in: J. Zhang (Ed.), *PEM Fuel Cell Electrocatalysts and Catalyst Layers: Fundamentals and Application*, Springer, 2008 (Chapter 14).
- [11] A. Kongkanand, Z. Liu, I. Dutta, F.T. Wagner, *J. Electrochem. Soc.* 158 (2011) B1286–B1291.
- [12] [http://www.hydrogen.energy.gov/pdfs/review09/fc\\_17\\_debe.pdf](http://www.hydrogen.energy.gov/pdfs/review09/fc_17_debe.pdf).
- [13] D.A. Stevens, S. Wang, R.J. Sanderson, A. Garsuch, M.K. Debe, S.M. Hendricks, R.T. Atanasoski, J.R. Dahn, *J. Electrochem. Soc.* 157 (2010) B737–B743.
- [14] M.K. Debe, S.M. Hendricks, G.D. Vernstrom, M. Meyers, M. Brostrom, M. Stephens, Q. Chan, J. Willey, M. Hamden, C.K. Mittelsteadt, C.B. Capuano, K.E. Ayers, E.B. Anderson, *J. Electrochem. Soc.* 159 (2012) K165–K176.
- [15] M. Howells, C. Jacobsen, T. Warwick, in: P.W. Hawkes, J.C.H. Spence (Eds.), *Science of Microscopy*, Springer, New York, 2007, pp. 835–926 (Chapter 13).
- [16] H. Ade, A.P. Hitchcock, *Polymer* 49 (2008) 643–675.
- [17] A.P. Hitchcock, in: G. van Tendeloo, D. van Dyck, S.J. Pennycook (Eds.), *Handbook of Nanoscopy*, vol. 2, Wiley, 2012, pp. 745–791 (Chapter 22).
- [18] D. Bessarabov, A.P. Hitchcock, *Membr. Technol.* 2009 (2009) 6–12.
- [19] D. Susac, J. Wang, Z. Martin, A.P. Hitchcock, J. Stumper, D. Bessarabov, *ECS Trans.* 33 (2010) 391–398.
- [20] V. Berejnov, Z. Martin, M. West, S. Kundu, D. Bessarabov, J. Stumper, D. Susac, A.P. Hitchcock, *Phys. Chem. Chem. Phys.* 14 (2012) 4835–4843.
- [21] V. Berejnov, D. Susac, J. Stumper, A.P. Hitchcock, *ECS Trans.* 41 (2011) 395–402.
- [22] D. Susac, V. Berejnov, A.P. Hitchcock, J. Stumper, *ECS Trans.* 41 (2011) 629–635.
- [23] D. Susac, V. Berejnov, A.P. Hitchcock, J. Stumper, *ECS Trans.* 50 (2012) 405–413.
- [24] V. Berejnov, D. Susac, J. Stumper, A.P. Hitchcock, *ECS Trans.* 50 (2012) 361–368.
- [25] V. Lee, D. Susac, S. Kundu, V. Berejnov, R.T. Atanasoski, A.P. Hitchcock, J. Stumper, *ECS Trans.* 58 (2013) 473–479.
- [26] K.V. Kaznatcheev, C. Karunakaran, U.D. Lanke, S.G. Urquhart, M. Obst, A.P. Hitchcock, *Nucl. Instrum. Methods Phys. Res. Sect. A* 582 (2007) 96–99.
- [27] A.L.D. Kilcoyne, T. Tyliczcak, W.F. Steele, S. Fakra, P. Hitchcock, K. Franck, E. Anderson, B. Harteneck, E.G. Rightor, G.E. Mitchell, A.P. Hitchcock, L. Yang, T. Warwick, H. Ade, *J. Synchrotron Radiat.* 10 (2003) 125–136.
- [28] T. Warwick, H. Ade, D. Kilcoyne, M. Kritscher, T. Tyliczcak, S. Fakra, A.P. Hitchcock, P. Hitchcock, H. Padmore, *J. Synchrotron Radiat.* 9 (2002) 254–257.
- [29] aXis2000 is written in Interactive Data Language, and is available free for non-commercial use at <http://unicorn.mcmaster.ca/aXis2000.html>.
- [30] J. Stöhr, *NEXAFS Spectroscopy*, Springer Series in Surface Sciences, vol. 25, Springer, Berlin, 1992.
- [31] J. Taborski, P. Väterlein, H. Dietz, U. Zimmermann, E. Umbach, *J. Electron Spectrosc. Relat. Phenom.* 75 (1995) 129–147.
- [32] H. Oji, R. Mitsumoto, E. Ito, H. Ishii, Y. Ouchi, K. Seki, N. Kosugi, *J. Electron Spectrosc. Relat. Phenom.* 78 (1996) 383–386.
- [33] I. Mori, T. Araki, H. Ishii, Y. Ouchi, K. Seki, K. Kondo, *J. Electron Spectrosc. Relat. Phenom.* 78 (1996) 371–374.
- [34] J. Stöhr, M.G. Samant, J. Lüning, A.C. Callegari, P. Chaudhari, J.P. Doyle, J.A. Lacey, S.A. Lien, S. Purushothaman, J.L. Speidell, *Science* 292 (2001) 2299–2301.
- [35] O. Benson Jr., M.K. Debe, B.E. Spiewak, US Patent 6136412A, 1997.
- [36] G.E. Mitchell, L.R. Wilson, M.T. Dineen, S.G. Urquhart, F. Hayes, E.G. Rightor, A.P. Hitchcock, H. Ade, *Macromolecules* 35 (2002) 1336–1341.
- [37] J.A. Brandes, G.D. Cody, D. Rumble, P. Haberstroh, S. Wirick, Y. Gelinas, *Carbon* 46 (2008) 1424–1434.
- [38] S.G. Rinaldo, W. Lee, J. Stumper, M. Eikerling, *Phys. Rev. E* 86 (2012) 041601.
- [39] J.P. Meyers, R.M. Darling, *J. Electrochem. Soc.* 153 (2006) A1432–A1442.
- [40] C.A. Reiser, L. Bregoli, T.W. Patterson, J.S. Yi, J.D. Yang, M.L. Perry, T.D. Jarvi, *Electrochem. Solid-State Lett.* 8 (2005) A273–A276.
- [41] D.F. van der Vliet, C. Wang, D. Tripkovic, D. Strmcnik, X.F. Zhang, M.K. Debe, R.T. Atanasoski, N.M. Markovic, V.R. Stamenkovic, *Nat. Mater.* 11 (2012) 1051–1058.